

Manuscript Template

Metallic line defect in wide-bandgap transparent perovskite BaSnO₃

45 Authors

Hwanhui Yun¹, Mehmet Topsakal², Abhinav Prakash^{1,3,4}, Bharat Jalan¹, Jong Seok Jeong^{1,5}, Turan Birol¹, K. Andre Mkhoyan^{1*}

Affiliations

- ¹ Department of Chemical Engineering and Materials Science, University of Minnesota, Minneapolis, MN 55455.
- ² Nuclear Science and Technology Department, Center for Functional Nanomaterials, Brookhaven National Laboratory, Upton, NY 11973.
- ³ Pritzker School of Molecular Engineering, University of Chicago, Chicago, IL 60637.
- ⁴ Center for Nanoscale Materials, Argonne National Laboratory, Lemont, IL 60439.
- ⁵ Analytical Sciences Center, LG Chem Ltd., Daeieon, Republic of Korea.

*Correspondence to: mkhoyan@umn.edu.

Abstract

A line defect with metallic characteristics has been discovered in optically transparent BaSnO₃ perovskite thin films. The distinct atomic structure of the defect core, comprised of Sn and O atoms, was visualized by atomic-resolution scanning transmission electron microscopy (STEM). When doped with La, dopants that replace Ba atoms preferentially segregate to specific crystallographic sites adjacent to the line defect. The electronic structure of the line defect probed in STEM with electron energy loss spectroscopy (EELS) was supported by *ab initio* theory, which indicates the presence of Fermi-level-crossing electronic bands that originate from defect core atoms. These metallic line defects also act as electron sinks attracting additional negative charges in these wide-bandgap BaSnO₃ film.

One Sentence Summary

A metallic line defect is found in wide-bandgap perovskite oxide thin films.

MAIN TEXT

363738

39

40

41

42

43

44

45

46

47

48

49

50

51

52

53

54

55

56

57

58

59

60

61

62

Introduction

In crystals, imperfections exist as various forms of defects covering a full dimensionality spectrum ranging from zero-dimensional (0D) point defects, such as vacancies and dopants; to more extended defects, such as one-dimensional (1D) dislocations and disclinations; twodimensional (2D) grain boundaries and stacking faults; and finally, three-dimensional (3D) voids and inclusions. Of particular interest for new technologies are extended 1D and 2D defects since they run across the macroscopic crystal in certain directions and are atomically small in others. Thus, they can provide nanoscale and, in some cases, atomic-scale tunability of material properties without altering the overall structure of the crystal (1). Perovskite crystals (ABX₃) have been shown to be suitable hosts for various conventional and nonconventional 1D and 2D defects with unexpected properties. A large diversity of elements can be incorporated at each of three A, B, and X sites of perovskites, engendering with a wide range of phases and functionalities (2-4). Since the structure of perovskites, especially perovskite oxides, are highly flexible, it accommodates various types of distortions including octahedral BO₆ tilt (5,6), uniaxial and biaxial strains (7), orbital ordering (8,9), and cation ordering (10). The structural flexibility of perovskites allows formation of unique extended defects such as intrusion of related phases, e.g. Ruddlesden-Popper faults and phases (11,12) or Aurivillius phase (13), nanorods, and line defects (14-16). Analytical atomic-resolution scanning transmission electron microscopes (STEM) equipped with various spectrometers (17-19) are uniquely suitable for discovery of new extended 1D and 2D defects and characterization of their atomic structure, composition, and electronic properties (15,20-22). Here, using STEM imaging, energy dispersive X-ray (EDX), and electron energy-loss spectroscopy (EELS), in combination with ab initio calculations, we report on the identification of a new kind 1D line defect with metallic characteristics in otherwise transparent, wide-bandgap perovskite BaSnO₃ thin films. While only a few non-conventional (not dislocation or disclination type) line defects have been reported, e.g. a semiconducting line defect in insulating NdTiO₃ (15), the field of non-conventional line defects in perovskites is still largely unexplored, but hugely promising.

Perovskite BaSnO₃ is one of the Alkaline-earth stannates (ASnO₃, A=Ca, Sr, and Ba) that has high optical transparency due to its wide bandgap of 3.0 ± 0.2 eV (23,24). It also has high room temperature carrier mobility, reaching $320 \text{ cm}^2\text{V}^{-1}\text{s}^{-1}$ in a doped BaSnO₃ bulk crystal (25,26) and $183 \text{ cm}^2\text{V}^{-1}\text{s}^{-1}$ in a doped BaSnO₃ thin film (27,28) despite the presence of a considerable amount of crystalline defects. Typical extended defects such as threading and misfit dislocations (28-30), grain boundaries (30), and Ruddlesden-Popper faults (29), are common in these perovskite BaSnO₃ films regardless of growth methods.

Results and Discussion

The findings discussed here come from STEM-based experiments conducted on La-doped BaSnO₃ (La:BaSnO₃) films. Films grown with two different techniques, high pressure oxygen sputtering and hybrid molecular beam epitaxy (MBE), were studied and almost all of them had the same metallic line defect in them. The low-magnification cross-sectional high-angle annular dark-field (HAADF)-STEM image of one of the La:BaSnO₃ films, grown on a LaAlO₃ substrate, shows the overall structure of the BaSnO₃ film (Fig. 1A). The contrast variations due to grain boundaries and dislocations can be seen throughout its thickness. At high-resolution, due to considerable differences in atomic numbers between cations Ba ($Z_{Ba} = 56$), Sn ($Z_{Sn} = 50$) and anion O ($Z_{O} = 8$), HAADF-STEM images only show the atomic columns with cations in them, as seen in Fig. 1B. Since perovskite BaSnO₃ has a cubic crystal structure, projected HAADF-STEM images recorded along all three major axes ([001], [010], and [100]) show the same atomic column arrangement, if the film is fully relaxed.

90 plan-vi
91 becaus
92 the cen
93 direction
94 along 1
95 defects

96

97

98

99

100

101

102

103

104

105

106

107

108

109

110

111

112

113

In the high-resolution HAADF-STEM images of these BaSnO₃ films obtained in plan-view, one of which is presented in Fig. 1C, the new line defects can be easily spotted because of their unique atomic configuration with a characteristic pair of atomic columns at the center. Interestingly, these line defects are observed only when viewed in the plan-view direction regardless of film growth technique, which indicates that they form preferentially along the growth direction suggesting possibilities for manipulations and control of the defects.

Atomic-resolution STEM-EDX elemental maps (Fig. 1D) reveal the compositional details of the defect core and its surrounding (for details, see SM Fig. S1). The two atomic columns at the center—the main visible feature of this defect—are Sn atomic columns (for additional examples of images and EDX maps of the line defects in sputtered and MBE grown films, see SM Fig. S2). To form the defect core, it appears two Ba columns should be absent and two Sn columns are 'rotated' 90 degrees along the [001] axis from their original (host) positions. Slight displacements of the four closest Ba columns toward the defect core to relax the strain in the structure are also observed (for details, see SM Fig. S3). Interestingly, high concentrations of La dopants are detected at the specific Ba sites adjacent to the line defect. As can be seen from La EDX map in Fig. 1D, La dopants are primarily substituting Ba atoms in the Ba columns just next to the core Sn-Sn pair, at the type (1) sites; and less frequently, in Ba columns next to those, at the type (2) sites (for more examples, see SM Fig. S2). When defect core Sn-Sn pair distance was measured and compared to that in the host BaSnO₃, which is the same as the lattice constant a_0 , it was found to be only about $0.61 \times a_0$ and had a range from $0.45 \times a_0$ to $0.75 \times a_0$ (Fig. 1E).

An illustration of these line defects inside a BaSnO₃ film formed along the film growth direction (*c*-axis) is shown in Fig. 2A. It should be noted that not all line defects necessarily propagate from a substrate to the film surface (see SM Fig. S4). Based on the

STEM observations, a one-unit-cell-thick model for a basic atomic structure of the line defect was constructed. Then, the model was relaxed to its lowest energy configuration by employing ab initio calculations (for details, see Materials and Methods). For better insight into the structure of this line defect, several models with slight structural and compositional variations were considered, relaxed, and evaluated: (i) without La dopants; (ii) with La dopants at sites (1), (2) and others; (iii) with and without oxygen in-between Sn-Sn pair in the core (for details, see SM Figs. S5,6). The final relaxed structure of the simplest and the most representative model for the line defect is shown in Fig. 2B viewed in three main projections. In this simplified model, La dopants are substituting all Ba atoms at the sites type (1) and the sites type (2) are free of La. Interestingly, after the structural relaxation, the two core Sn atomic columns are shifted a half-unit cell along the line defect direction ([001]), which is visible when viewed from [100] and [010] directions. The distance between core Sn-Sn atomic columns is also reduced and four adjacent Ba columns are moved inward, both of which are consistent with the experimental observations (see also SM Fig. S3). The agreement between this model and STEM measurements appears to be fairly good including a close match of the core Sn-Sn distance in the relaxed structure $(0.72 \times a_0)$ to experimentally observed values.

114

115

116

117

118

119

120

121

122

123

124

125

126

127

128

129

130

131

132

133

134

135

136

137

138

Using this simple model for atomic structure, the electronic band structure of the line defect was calculated using density functional theory (DFT) and, interestingly, defect-induced electronic bands crossing the Fermi level, E_F , were observed, as illustrated in Fig. 2C. The resulting band structure along with total and atom-projected density of states (DOS) are shown in Fig. 2D. A few defect-induced electronic bands (highlighted in red) are partially filled as they cross the Fermi level, $E_F = 0$, which implies the presence of metallic electronic states in the line defect. In addition to these bands, there are also other unfilled, defect-induced, distinct bands spanning from 0.2 eV to 1.3 eV that are not present in bulk

BaSnO₃ (31). While atom-projected DOS reveals that the metallic states are originated from O and Sn atoms in the structure (Fig. 2D), site-projected DOS of individual Sn and O atoms in the structure helps to identify the sites responsible for metallic bands. As shown in Fig. 2E, the metallic bands that are crossing the Fermi level are, indeed, originated primarily from Sn and O atoms in the defect core: Sn-1, O-1, O-2, and O-3. These results appear to be the direct consequence of considerable differences between the coordination and bond angles for the core O and Sn atoms than those in the host perovskite BaSnO₃ (e.g. Sn-O-Sn angle is 74° and 58° in core and 180° in host). Electronic structure calculations conducted for the line defect without La dopants (see SM Fig. S7) and for the line defect with an O vacancy (see SM Fig. S8) also showed a metallic defect core with similar results for band structure and DOS, suggesting that being metallic is most likely an intrinsic property of these line defects in BaSnO₃.

Since these metallic line defects are imbedded inside an n-type doped insulating BaSnO₃ host (32) (each La dopant provides one extra electron when it substitutes Ba atom), some changes in atomic and electronic structures are expected when an extra negative charge is introduced into the system. A set of calculations for structure optimization with different amounts of added negative charge (number of electrons) was performed. It revealed that an increase of additional negative charge decreases the Sn-Sn distance at the core, bringing the structure even closer to the ones observed in experiments (Fig. 3A). A reduction of core Sn-Sn distance was observed for both line defects with and without La dopants. Since the line defects in the different films have different amounts of surrounding dopants and additional negative charges in them, that would explain the experimentally-observed variation of Sn-Sn distances in the core discussed earlier (Fig. 1E).

The electron density distributions of these negatively-charged line defects were calculated and compared with those of the original line defect to visualize the sites where

the additional charge accumulates. The electron density maps for La-doped line defects with and without two added electrons were calculated using relaxed atomic structures with additional electrons; then an electron density difference map (EDDM) was constructed. The EDDMs for the two crystalline planes (BaO and SnO₂ planes) perpendicular to the defect line are shown in Fig. 3B. They indicate that the additional electrons are filling the available states in the Sn and O atoms at the defect core, which is consistent with their metallic characteristics – having localized electronic states that are crossing the Fermi level. These line defects appear to act as electron sinks attracting additional negative charges in the film. The EDDMs also provide a real-space visualization of the changes in the electronic orbitals of the atoms that are contributing to the band structure. The characteristic lobes of filled O 2p orbitals are clearly visible in EDDM of the SnO₂ plane (Fig. 3B), where the effects of the orbital hybridization due to bonding are minimal. The EDDMs calculated for the line defect without La dopants, which is also metallic, show similar defect-core-concentrated distribution of the additional electrons (see SM Fig. S9).

EELS core-loss edges are directly related to the local DOS above the Fermi energy of the material and can be acquired in STEM at atomic-resolution in parallel with imaging (33,34), therefore, it is an excellent method for experimental investigation of the local electronic structure of extended 1D and 2D defects. To determine the applicability of the core-level EELS for this new line defect, the spectral shapes of O K edge, the most sensitive EELS edge in BaSnO₃, were simulated for different oxygen atoms in the line defect structure. The calculations were based on electronic band structure and DOS (Figs. 2D,E) with incorporation of the core-hole effect. The results, presented in Fig. 4A, indicate that the K edge fine structures of the oxygen atoms at the defect sites are drastically different. In particular, three oxygen atoms at the defect core (sites O-1, O-2, and O-3 in Fig. 4A) exhibit a peak at the edge onset, which is due to metallic states in the band structure crossing the

Fermi energy, as discussed earlier. This and other visible changes in *K* edge fine structures of oxygen atoms in the defect core suggest that experimental EELS should be applicable here. However, due to STEM probe channeling and broadening *(35)* during its propagation through the sample (Fig. 4B), some intermixing of these simulated O *K* edges is expected in measured EELS data.

189

190

191

192

193

194

195

196

197

198

199

200

201

202

203

204

205

206

207

208

209

210

211

212

213

EELS O K edges were acquired across the line defects along two perpendicular directions: vertical (i) and parallel (ii) to the characteristic core Sn-Sn pair (Fig. 4C). The changes in the O K edge fine structures are localized within a few unit cells from the defect. For O K edges acquired along direction i, the changes in the fine structure at the defect core (region i0) relative to that of host BaSnO₃ (bulk, b) are readily observed. They are more pronounced in the difference spectrum (Fig. 4C). For comparison, the difference spectrum between the O K edges from the region i3, a three-unit-cell away from the core, and bulk shows only noise signals. At the defect core, the intensity near the onset (shaded 530–533.5 eV range) is enhanced, which is consistent with the presence of metallic states at the defect and with simulated edge predictions. In addition, peaks at 538.6 eV, 539.9 eV, 542.5 eV, and 545.0 eV present in the host crystal are dampened at the defect core, which is also consistent with simulated O K edges (Fig. 4A). EELS data acquired along the direction ii show similar results due to beam broadening and the intermixing of O K edges. The only difference here is in the region ii1, where the presence of La dopants causes formation of new electronic states around 5 eV above the Fermi level at neighboring oxygen atoms (sites O-4 and O-5, in Fig. 4A).

When the difference spectrum from measured and simulated O K edges are compared (Fig. 4C), a good agreement is observed. The simulated O K edges used here for direct comparison with measured edges include effects of intermixing due to beam channeling and broadening (for details, see SM Fig. S10). It should be noted that an even

better match with experimental data might be achieved if simulated O K edges not only were based on the simple model of the line defect with two La dopants (Fig. 2B), but also include what was observed in actual films, that is, some portion of the defect does not have dopants at all and some La dopants are on other sites (Fig. 1D); and extra electrons can be accumulated at the defect core. Again, the simple model of the line defect appears to be sufficient to describe the essential properties of this metallic line defect.

The discovery of oxide metallic line defects in otherwise wide-bandgap transparent perovskite BaSnO3 films demonstrates that extended 1D defects can accommodate remarkable properties and provide unique means for engineering material properties at sub-nm length scale. Controlling the distribution, and orientations of such line defects offers exciting new opportunities for developing superior crystalline materials with extraordinary properties, including unidirectional metallic conductivity with simultaneous insulating character in orthogonal directions. Exploration of extended 1D defects beyond dislocations in perovskites is a mostly uncharted field where unexpected defect properties and new physical phenomena at atomic dimensions are waiting to be discovered.

Materials and Methods

STEM characterization

La:BaSnO₃ films were grown on a LaAlO₃(001)_{pc} substrate by using high pressure oxygen sputter deposition *(36)* and on LaAlO₃(001)_{pc} and SrTiO₃(001) substrates by hybrid molecular beam epitaxy *(37)*. La:BaSnO₃ films were grown on pseudo-cubic LaAlO₃ (001)_{pc} and SrTiO₃(001) substrates. Plan-view STEM samples were prepared by mechanical polishing (using MultiprepTM Allied High Tech, Inc.) followed by colloidal polishing with alumina abrasives to thin the foil and to reduce damaged layers on the surfaces. The thickness of the area for STEM experiments was 40–90 nm and ~40 nm for plan-view and cross-sectional view samples, respectively. Cross-sectional TEM samples were prepared by

the focus ion-beam (FIB) lift-out method using 30 kV Ga ion beam followed by ion shower at 2 kV Ga ion beam.

STEM experiments were performed using aberration-corrected FEI Titan G2 60-300 (S)TEM equipped with a CEOS DCOR probe corrector, a Schottky extreme field emission gun (X-FEG), a monochromator, a super-X energy dispersive X-ray detector, and a Gatan Enfinium ER spectrometer. The microscope was operated at 200 keV and screen current of 25-30 pA. STEM images and EDX elemental map were acquired using the probe semiconvergent angle of 17.3 mrad and ADF detector inner angles of 55 and 11 mrad for HAADF- and annular bright-field (ABF)-STEM images, respectively. STEM-EELS analysis was conducted using a monochromated probe allowing the energy resolution of 0.13 eV at the energy dispersion of 0.01 eV. The core-loss O K edges were acquired using the energy dispersion of 0.1 eV. Probe semi-convergent angle was 19 mrad and EELS collection angle was 29 mrad. Dual EELS mode was used to acquire the low-loss energy region with zero-loss peak (ZLP) and the high-loss energy region simultaneously, which allows energy drift correction using the ZLP alignment. The thicknesses of samples were determined from measured low-loss EELS spectra employing the log-ratio method with the mean free paths of plasmon excitation: $\lambda_p = 81$ nm for BaSnO₃ (38).

DFT simulations

239

240

241

242

243

244

245

246

247

248

249

250

251

252

253

254

255

256

257

258

259

260

261

262

263

The defect structure was obtained by fully relaxing the atomic coordinates and the lattice vectors, using the variable cell (vc-relax) option implemented in the Quantum-Espresso program package (39). Initial line defect structure was constructed using the supercell of $5\times4\times1$ u.c., where two Ba atoms were removed and two Sn atoms were displaced by 90° rotation along the [001] axis at the center of the supercell. Ultrasoft pseudopotentials (40) and a generalized gradient approximation (GGA) using Perdew-Burke-Ernzenhof (PBE)

parameterization for an exchange-correlation functional were employed (41). Kinetic energy cutoff for wavefunctions and for charge density were 50 Ry and 200 Ry, respectively. Relaxation was achieved by converging the forces on all atoms to less than 1×10^{-4} a.u. A k-points grid of $2\times2\times6$ was used. Atomic structure visualization in figures were performed using VESTA software (42).

Electronic structures and EELS simulations for the relaxed structures were carried out using the WIEN2K code (43-45). GGA-PBE parameterization was adopted for the electronic exchange-correlation functional (41). The Brillouin zone was sampled using a 4×4×16 shifted k-point grid. R_{MT} (Muffin-tin radii) that was automatically set by the code was used, which were 2.45 Å (the structure without La dopant) and 2.5 Å (the structure with La dopant) for Ba, 2.04 Å for Sn, 1.75 Å for O, and 2.49 Å for La. The basis set cut-off wave vector, k_{max} , was determined by the criterion $R_{min}k_{max} = 7$. Ground state electronic structures for charged line defects were calculated by adding electrons and adding corresponding background charge. Spin-orbit interactions were also included. EELS O K edge simulations were performed by using the TELNES3 module in WIEN2K with parameters identical to the experimental setup. To include the core-hole effects (46,47), the bigger supercell structure for the line defect was generated by doubling the relaxed line structures in the [001] direction, which is compatible to the size of $5\times4\times2$ u.c., and then, core-hole was incorporated in an absorbing oxygen atom. O K edge for the host BaSnO₃ (bulk) was computed using the BaSnO₃ supercell with a size of 5×4×2 u.c. The natural energy broadening of the core edges, caused by the life time of the electrons in the initial and final states of excitation, was incorporated as well (38,48,49).

STEM simulations

264

265

266

267

268

269

270

271

272

273

274

275

276

277

278

279

280

281

282

283

284

285

286

287

288
289
290
291
292
293
294
295
296
297

299

300

STEM image and STEM probe propagation simulations were performed using the TEMSIM code based on the *Multislice* method (50-52). To simulate the HAADF- and ABF-STEM images of the line defect, the relaxed line defect structure with two La dopants was used, which has the supercell size of a = 21.01 Å, b = 16.53 Å, and c = 4.11 Å. The STEM probe parameters were set to be: beam energy of 200 keV, a convergence angle of 17.3 mrad (STEM image) and 19 mrad (electron beam propagation), $C_s = 0$, and slice thickness of 2.055 Å. Thermal diffuse scattering was included using frozen-phonon approximation for T = 300 K (51). Root-mean square thermal displacements were set as 0.095 Å for Ba, 0.1 Å for Sn, 0.089 Å for O, and 0.041 Å for La (53). Inner/outer detector angles for the HAADF-and ABF- STEM images were 50/200 mrad and 10/40 mrad. The computed STEM images were convoluted with a Gaussian function with the full-width-at-half-maximum of 0.8 Å to incorporate the source size (54).

Science Advances Manuscript Template Page 12 of 24

References

301

304

305

- 1. B. G. Yacobi, D. B. Holt, *Extended Defects in Semiconductors*. (Cambridge University Press, Cambridge, UK, 2007).
 - 2. J. B. Goodenough, Electronic and ionic transport properties and other physical aspects of perovskites. *Rep. Prog. Phys.* **67**, 1915-1993 (2004).
- 3. H. N. Lee, H. M. Christen, M. F. Chisholm, C. M. Rouleau, D. H. Lowndes,

 Strong polarization enhancement in asymmetric three-component ferroelectric

 superlattices. *Nature* **433**, 395-399 (2005).
- D. Lee, H. Lu, Y. Gu, S.-Y. Choi, S.-D. Li, S. Ryu, T. R. Paudel, K. Song, E.
 Mikheev, S. Lee, S. Stemmer, D. A. Tenne, S. H. Oh, E. Y. Tsymbal, X. Wu, L.-Q. Chen,
 A. Gruverman, C. B. Eom, Emergence of room-temperature ferroelectricity at reduced
 dimensions. *Science* 349, 1314-1317 (2015).
- 5. T. H. Kim, D. Puggioni, Y. Yuan, L. Xie, H. Zhou, N. Campbell, P. J. Ryan, Y. Choi, J. W. Kim, J. R. Patzner, S. Ryu, J. P. Podkaminer, J. Irwin, Y. Ma, C. J. Fennie, M. S. Rzchowski, X. Q. Pan, V. Gopalan, J. M. Rondinelli, C. B. Eom, Polar metals by geometric design. Nature **533**, 68-72 (2016).
- T. Nan, T. J. Anderson, J. Gibbons, K. Hwang, N. Campbell, H. Zhou, Y. Q.
 Dong, G. Y. Kim, D. F. Shao, T. R. Paudel, N. Reynolds, X. J. Wang, N. X. Sun, E. Y.
 Tsymbal, S. Y. Choi, M. S. Rzchowski, Y. B. Kim, D. C. Ralph, C. B. Eom, Anisotropic
 spin-orbit torque generation in epitaxial SrIrO₃ by symmetry design. *Proc. Natl. Acad. Sci.* 116, 16186-16191 (2019).
- J. H. Haeni, P. Irvin, W. Chang, R. Uecker, P. Reiche, Y. L. Li, S. Choudhury, W.
 Tian, M. E. Hawley, B. Craigo, A. K. Tagantsev, X. Q. Pan, S. K. Streiffer, L. Q. Chen, S.
 W. Kirchoefer, J. Levy, D. G. Schlom, Room-temperature ferroelectricity in strained
 SrTiO₃. *Nature* 430, 758-761 (2004).

Science Advances Manuscript Template Page 13 of 24

- 326 8. Y. Yuan, Y. Lu, G. Stone, K. Wang, C. M. Brooks, D. G. Schlom, S. B. Sinnott, H.
- Zhou, V. Gopalan, Three-dimensional atomic scale electron density reconstruction of
- octahedral tilt epitaxy in functional perovskites. *Nat. Commun.* **9**, 5220 (2018).
- 9. J. B. Goodenough, J. S. Zhou, Orbital ordering in orthorhombic perovskites. *J.*
- 330 *Mater. Chem.* 17, 2394-2405 (2007).
- 331 10. G. King, P. M. Woodward, Cation ordering in perovskites. J. Mater. Chem. 20,
- 332 5785-5796 (2010).
- 11. C.-H. Lee, N. D. Orloff, T. Birol, Y. Zhu, V. Goian, E. Rocas, R. Haislmaier, E.
- Vlahos, J. A. Mundy, L. F. Kourkoutis, Y. Nie, M. D. Biegalski, J. Zhang, M. Bernhagen,
- N. A. Benedek, Y. Kim, J. D. Brock, R. Uecker, X. X. Xi, V. Gopalan, D. Nuzhnyy, S.
- Kamba, D. A. Muller, I. Takeuchi, J. C. Booth, C. J. Fennie, D. G. Schlom, Exploiting
- dimensionality and defect mitigation to create tunable microwave dielectrics. *Nature* **502**,
- 338 532-536 (2013).
- 339 12. G. Stone, C. Ophus, T. Birol, J. Ciston, C.-H. Lee, K. Wang, C. J. Fennie, D. G.
- Schlom, N. Alem, V. Gopalan, Atomic scale imaging of competing polar states in a
- Ruddlesden–Popper layered oxide. *Nat. Commun.* 7, 12572 (2016).
- 342 13. B. Frit, J. P. Mercurio, The crystal chemistry and dielectric properties of the
- Aurivillius family of complex bismuth oxides with perovskite-like layered structures. J.
- 344 Alloys Compd. 188, 27-35 (1992).
- 14. I. MacLaren, L. Q. Wang, B. Schaffer, Q. M. Ramasse, A. J. Craven, S. M.
- Selbach, N. A. Spaldin, S. Miao, K. Kalantari, I. M. Reaney, Novel nanorod precipitate
- formation in neodymium and titanium codoped bismuth ferrite. Adv. Funct. Mater. 23,
- 348 683-689 (2013).
- 15. J. S. Jeong, M. Topsakal, P. Xu, B. Jalan, R. M. Wentzcovitch, K. A. Mkhoyan, A
- new line defect in NdTiO₃ Perovskite. *Nano Lett.* **16**, 6816-6822 (2016).

Science Advances Manuscript Template Page 14 of 24

- 16. C. Li, D. Song, M. Li, C. Tang, D. Xue, D. Wan, S. J. Pennycook, Atomic scale characterization of point and extended defects in niobate thin films. *Ultramicroscopy* **203**,
- 353 82-87 (2019).

- 17. M. Bosman, V. J. Keast, J. L. García-Muñoz, A. J. D'Alfonso, S. D. Findlay, L. J.
- Allen, Two-Dimensional Mapping of Chemical Information at Atomic Resolution. *Phys.*
- 356 Rev. Lett. **99**, 086102 (2007).
- 18. D. A. Muller, L. F. Kourkoutis, M. Murfitt, J. H. Song, H. Y. Hwang, J. Silcox, N.
- Dellby, O. L. Krivanek, Atomic-scale chemical imaging of composition and bonding by
- aberration-corrected microscopy. *Science* **319**, 1073-1076 (2008).
- 360 19. A. J. D'Alfonso, B. Freitag, D. Klenov, L. J. Allen, Atomic-resolution chemical
- mapping using energy-dispersive x-ray spectroscopy. *Phys. Rev. B* **81**, 100101 (2010).
- 362 20. R. F. Klie, J. P. Buban, M. Varela, A. Franceschetti, C. Jooss, Y. Zhu, N. D.
 - Browning, S. T. Pantelides, S. J. Pennycook, Enhanced current transport at grain
- boundaries in high-Tc superconductors. *Nature* **435**, 475-478 (2005).
- 21. Z. Zhang, W. Sigle, W. Kurtz, HRTEM and EELS study of screw dislocation cores
- in SrTiO₃. Phys. Rev. B **69**, 144103 (2004).
- 22. P. Gao, R. Ishikawa, B. Feng, A. Kumamoto, N. Shibata, Y. Ikuhara, Atomic-scale
- structure relaxation, chemistry and charge distribution of dislocation cores in SrTiO₃.
- 369 *Ultramicroscopy* **184**, 217-224 (2018).
- 370 23. H. J. Kim, U. Kim, T. H. Kim, J. Kim, H. M. Kim, B.-G. Jeon, W.-J. Lee, H. S.
- Mun, K. T. Hong, J. Yu, K. Char, K. H. Kim, Physical properties of transparent perovskite
- oxides (Ba,La)SnO₃ with high electrical mobility at room temperature. *Phys. Rev. B* **86**,
- 373 165205 (2012).

Science Advances Manuscript Template Page 15 of 24

- 374 24. S. A. Chambers, T. C. Kaspar, A. Prakash, G. Haugstad, B. Jalan, Band alignment
- at epitaxial BaSnO₃/SrTiO₃(001) and BaSnO₃/LaAlO₃(001) heterojunctions. *Appl. Phys.*
- 376 *Lett.* **108**, 152104 (2016).
- 377 25. X. Luo, Y. S. Oh, A. Sirenko, P. Gao, T. A. Tyson, K. Char, S.-W. Cheong, High
- carrier mobility in transparent Ba_{1-x}La_xSnO₃ crystals with a wide band gap. *Appl. Phys.*
- 379 *Lett.* **100**, 172112 (2012).

390

- 380 26. H. J. Kim, U. Kim, H. M. Kim, T. H. Kim, H. S. Mun, B.G. Jeon, K. T. Hong, W.
- J. Lee, C. Ju, K. H. Kim, K. Char, High mobility in a stable transparent perovskite oxide.
- 382 *Appl. Phys. Express* **5**, 061102 (2012).
- 383 27. S. Raghavan, T. Schumann, H. Kim, J. Y. Zhang, T. A. Cain, S. Stemmer, High-
- mobility BaSnO₃ grown by oxide molecular beam epitaxy. APL Mater. 4, 016106 (2016).
- 385 28. H. Paik, Z. Chen, E. Lochocki, A. S. H., A. Verma, N. Tanen, J. Park, M. Uchida,
 - S. Shang, B.-C. Zhou, M. Brützam, R. Uecker, Z.-K. Liu, D. Jena, K. M. Shen, D. A.
- Muller, D. G. Schlom, Adsorption-controlled growth of La-doped BaSnO₃ by molecular-
- 388 beam epitaxy. APL Mater. 5, 116107 (2017).
- 389 29. W. Y. Wang, Y. L. Tang, Y. L. Zhu, J. Suriyaprakash, Y. B. Xu, Y. Liu, B. Gao, S.
 - W. Cheong, X. L. Ma, Atomic mapping of Ruddlesden-Popper faults in transparent
- conducting BaSnO₃-based thin films. Sci. Rep. **5**, 16097 (2015).
- 392 30. H. Yun, K. Ganguly, W. Postiglione, B. Jalan, C. Leighton, K. A. Mkhoyan, J. S.
- Jeong, Microstructure characterization of BaSnO₃ thin films on LaAlO₃ and PrScO₃
- substrates from transmission electron microscopy. *Sci. Rep.* **8**, 10245 (2018).
- 31. E. Moreira, J. M. Henriques, D. L. Azevedo, E. W. S. Caetano, V. N. Freire, U. L.
- Fulco, E. L. Albuquerque, Structural and optoelectronic properties, and infrared spectrum
- of cubic BaSnO₃ from first principles calculations. J. Appl. Phys. **112**, 043703 (2012).

Science Advances Manuscript Template Page 16 of 24

- 32. A. Prakash, P. Xu, A. Faghaninia, S. Shukla, J. W. Ager III, C. S. Lo, B. Jalan,
 Wide bandgap BaSnO₃ films with room temperature conductivity exceeding 10⁴ Scm⁻¹,

 Nat. Commun. 8, 15167 (2017).
- 33. D. A. Muller, D. J. Singh, J. Silcox, Connections between the electron-energy-loss spectra, the local electronic structure, and the physical properties of a material: A study of nickel aluminum alloys. *Phys. Rev. B* **57**, 8181-8202 (1998).

405

406

407

408

409

410

411

412

413

414

415

416

417

419

- 34. L. J. Allen, S. D. Findlay, M. P. Oxley, "Simulation and Interpretation of Images" in *Scanning Transmission Electron Microscopy: Imaging and Analysis*, S. J. Pennycook, P. D. Nellist, Eds. (Springer, New York, NY, USA 2011), pp. 247-289.
 - 35. R. J. Wu, A. Mittal, M. L. Odlyzko, K. A. Mkhoyan, Simplifying electron beam channeling in scanning transmission electron microscopy. *Microsc. Microanal.* **23**, 794-808 (2017).
- 36. K. Ganguly, P. Ambwani, P. Xu, J. S. Jeong, K. A. Mkhoyan, C. Leighton, B. Jalan, Structure and transport in high pressure oxygen sputter-deposited BaSnO_{3-δ}. *APL Mater.* **3**, 062509 (2015).
 - 37. A. Prakash, J. Dewey, H. Yun, J. S. Jeong, K. A. Mkhoyan, B. Jalan, Hybrid molecular beam epitaxy for the growth of stoichiometric BaSnO₃. *J. Vac. Sci. Technol. A* 33, 060608 (2015).
 - 38. R. F. Egerton, *Electron Energy Loss Spectroscopy in the Electron Microscope* (third edition, Springer, New York, NY, USA, 2011).
- 418 39. P. Giannozzi, S. Baroni, N. Bonini, M. Calandra, R. Car, C. Cavazzoni, D.
 - Ceresoli, G. L. Chiarotti, M. Cococcioni, I. Dabo, A. Dal Corso, S. de Gironcoli, S. Fabris,
- G. Fratesi, R. Gebauer, U. Gerstmann, C. Gougoussis, A. Kokalj, M. Lazzeri, L. Martin-
- Samos, N. Marzari, F. Mauri, R. Mazzarello, S. Paolini, A. Pasquarello, L. Paulatto, C.
- Sbraccia, S. Scandolo, G. Sclauzero, A. P. Seitsonen, A. Smogunov, P. Umari, R. M.

Science Advances Manuscript Template Page 17 of 24

- Wentzcovitch, QUANTUM ESPRESSO: a modular and open-source software project for
- 424 quantum simulations of materials. J. Phys. Condens. Matter 21, 395502 (2009).
- 425 40. K. F. Garrity, J. W. Bennett, K. M. Rabe, Pseudopotentials for high-throughput
- 426 DFT calculations. *Comput. Mater. Sci.* **81**, 446-452 (2014).
- 41. J. P. Perdew, K. Burke, M. Ernzerhof, Generalized gradient approximation made
- 428 simple. *Phys. Rev. Lett.* **77**, 3865-3868 (1996).
- 42. I. F. Momma Koichi, VESTA3 for three-dimensional visualization system for
- crystallographic studies and electronic state calculations. J. Appl. Crystallogr. 44, 5
- 431 (2011).
- 432 43. K. Schwarz, P. Blaha, G. K. H. Madsen, Electronic structure calculations of solids
- using the WIEN2k package for material sciences. Comput. Phys. Comm. 147, 71-76
- 434 (2002).
- 435 44. K. Schwarz, P. Blaha, Solid state calculations using WIEN2k. *Comput. Mater. Sci.*
- **28**, 259-273 (2003).
- 437 45. K. S. Peter Blaha, G. Madsen, D. Kvasnicka, J. Luitz, WIEN2k User's guide.
- 438 (Vienna University of Technology, Vienna, Austria, 2014).
- 439 46. C. Hébert, J. Luitz, P. Schattschneider, Improvement of energy loss near edge
- structure calculation using Wien2k. *Micron* **34**, 219-225 (2003).
- 441 47. C. Hébert, Practical aspects of running the WIEN2k code for electron
- spectroscopy. *Micron* **38**, 12-28 (2007).
- 48. M. O. Krause, Atomic radiative and radiationless yields for K and L shells. J.
- 444 Phys. Chem. Ref. Data 8, 307-327 (1979).
- 445 49. H. Yun, M. Topsakal, A. Prakash, K. Ganguly, C. Leighton, B. Jalan, R. M.
- Wentzcovitch, K. A. Mkhoyan, J. S. Jeong, Electronic structure of BaSnO₃ investigated by

Science Advances Manuscript Template Page 18 of 24

- high-energy-resolution electron energy-loss spectroscopy and ab initio calculations. *J. Vac. Sci. Technol. A* **36**, 031503 (2018).
- 50. J. M. Cowley, A. F. Moodie, The scattering of electrons by atoms and crystals. I. A new theoretical approach. *Acta Crystallogr.* **10**, 10 (1957).
 - 51. E. J. Kirkland, *Advanced Computing in Electron Microscopy*. (Springer, Boston, MA, USA, (2010).
 - 52. R. F. Loane, E. J. Kirkland, J. Silcox, Visibility of single heavy atoms on thin crystalline silicon in simulated annular dark-field STEM images. *Acta Crystallogr. A* **44**, 912-927 (1988).
 - 53. B. C. Chakoumakos, Systematics of atomic displacement parameters in perovskite oxides. *Physica B: Condens. Matter* **241**, 361-363 (1997).
 - 54. J. S. Jeong, M. L. Odlyzko, P. Xu, B. Jalan, K. A. Mkhoyan, Probing core-electron orbitals by scanning transmission electron microscopy and measuring the delocalization of core-level excitations. *Phys. Rev. B* **93**, 165140 (2016).

Acknowledgements

We would like to thank Dr. Koustav Ganguly and Prof. Chris Leighton for providing high pressure oxygen sputtered samples. **Funding:** This work is supported in part by SMART, one of seven centers of nCORE, a Semiconductor Research Corporation program, sponsored by National Institute of Standards and Technology (NIST), and by National Science Foundation (NSF) through University of Minnesota (UMN) MRSEC under Awards DMR-1420013 and DMR-2011401. This work utilized the UMN Characterization Facility, supported in part by the NSF through the UMN MRSEC program. The MBE growth work was supported partially by the NSF through DMR-1741801 and the Air Force Office of Scientific Research Program through grant no. FA9550-19-1-0245. **Author contributions:** H.Y. and K.A.M conceived the project. H.Y. performed STEM experiments and *Multislice*

simulations with inputs from J.S.J. and K.A.M., and *ab initio* calculations with inputs from M.T. and T.B. A.P. grew thin films by hybrid MBE with input from B.J. H.Y. and K.A.M. prepared the manuscript with contributions from all authors. K.A.M. directed all aspects of the project. **Competing interests:** The authors declare that they have no competing interests. **Data and materials availability:** All data needed to evaluate the conclusions in the paper are present in the paper and/or the Supplementary Materials. Additional data related to this paper may be requested from the authors.

Supplementary Materials:

Figures S1-S10

Figures

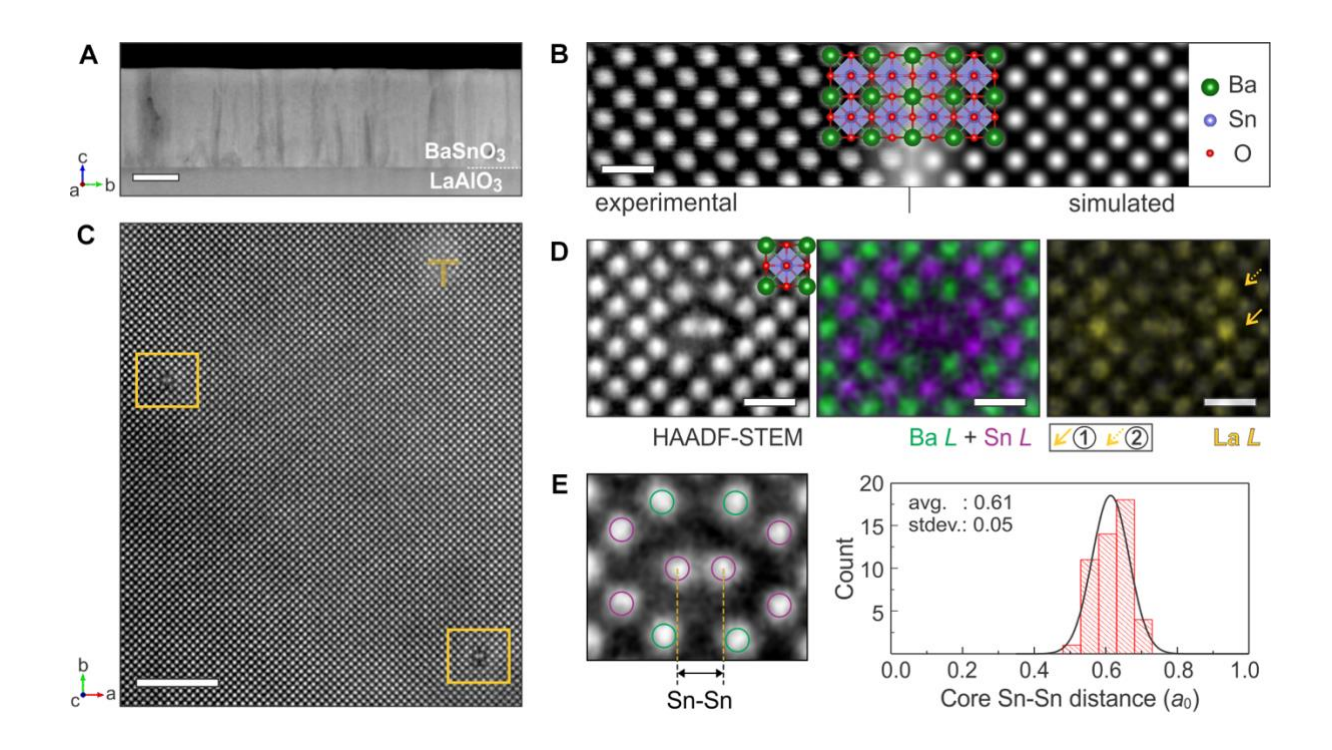


Fig. 1. HAADF-STEM images and EDX elemental maps of the line defect in perovskite BaSnO₃. (A) Cross-sectional HAADF-STEM image of a BaSnO₃ film grown on LaAlO₃ substrate. The scale bar is 100 nm. (B) Experimental and simulated atomic-resolution HAADF-STEM image of cubic BaSnO₃ viewed in the [001] direction. The overlaid polyhedral model shows the locations of the atoms in this projection. The scale bar is 0.5 nm. (C) Plan-view HAADF-STEM image of the BaSnO₃ film with two new line defects (in the yellow boxes) and one edge dislocation (indicated by a dislocation symbol). The scale bar is 4 nm. (D) High-magnification HAADF-STEM image and EDX elemental maps superimposed on the HAADF-STEM image. Here, the sum of eight cross-correlated elemental maps is shown. The scale bars are 0.5 nm. (E) A close-up image of the defect core and histogram of the core Sn-Sn column distances relative to the lattice constant (ao) of the host BaSnO₃. The histogram is compiled from individual line defects across many samples. Precision of individual Sn-Sn distance measurement is $\pm 0.04ao$.

Science Advances Manuscript Template Page 21 of 24

ones with metallic characteristics.

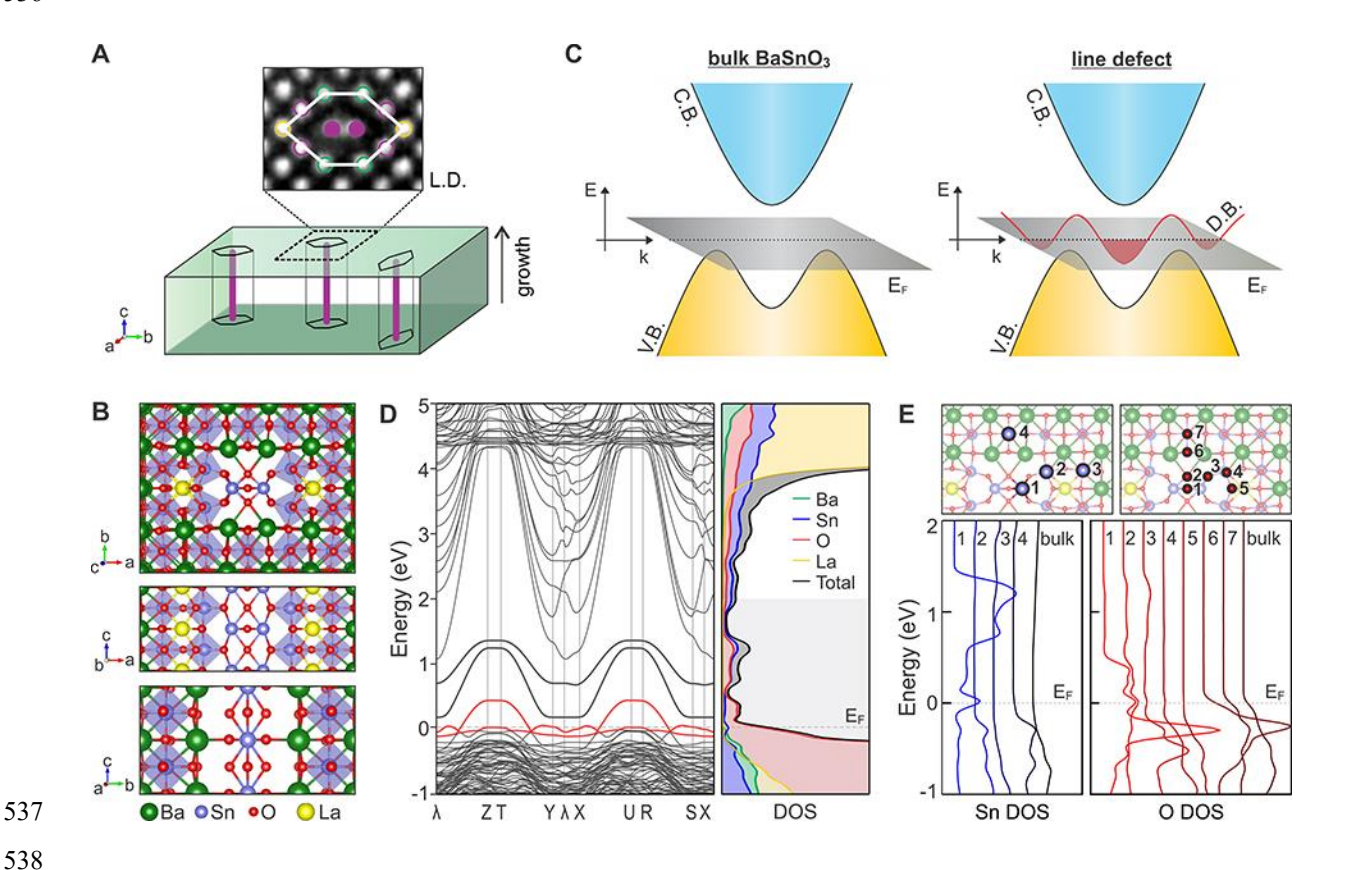


Fig. 2. Computed atomic and electronic structures of the line defect. (A) An illustration of line defects in BaSnO₃ thin film forming along the film growth direction. (B) Calculated atomic structure of the line defect viewed along the three major axes. Here La atoms acting as substitutional dopants are shown in yellow occupying Ba sites neighboring the defect core. The Sn atoms in the defect core are shifted a half unit cell along the defect line direction. The calculations also predict minor changes in the atomic structure of the BaSnO₃ structure outside defect core (e.g., an octahedral tilt in the four surrounding four SnO₆ octahedras when viewed in the *c*-direction). (C) Schematic band diagrams of BaSnO₃ illustrating the band from the line defect crossing E_F. (D) Electronic band structures and DOS of the line defect calculated using atomic structure in (B). Metallic bands, the bands that are crossing Fermi energy ($E_F = 0$), are highlighted in red. Atomprojected DOS indicate that the metallic bands are predominantly from O and Sn atoms. (E) Siteprojected DOS for Sn and O atoms in the line defect structure. The DOS of selected atoms, locations of which are indicated in the schematics on the top, show the O and Sn atoms of defect core are the

Science Advances Manuscript Template Page 22 of 24

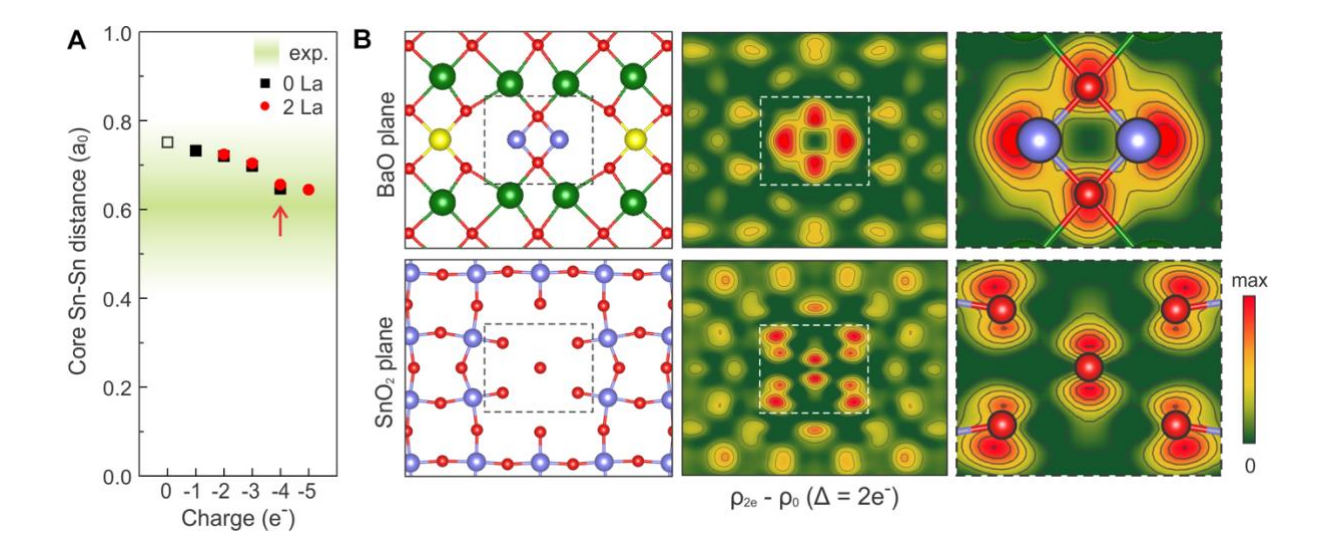


Fig. 3. The effect of additional negative charge on the line defect. (A) Calculated core Sn-Sn distance of the line defect as a function of negative charge added to the structure. Both cases, undoped (0 La) and La substitutional doped (2 La), are considered. In doped case, the structure already has $2e^{-}$ charge because each La ($Z_{La} = 57$) introduces one extra electron when it substitutes Ba ($Z_{Ba} = 56$). (B) The atomic arrangements (on the left) and corresponding electron density difference maps (EDDM) between the additionally-charged (with $2e^{-}$) and original line defects for both atomic planes perpendicular to the defect line direction (on the right). Magnified EDDMs of the defect core with overlaid atom positions show that most of the additional charge is concentrated at the core O and Sn atoms. The structure used for calculating these EDDMs is indicated by the arrow in (A).

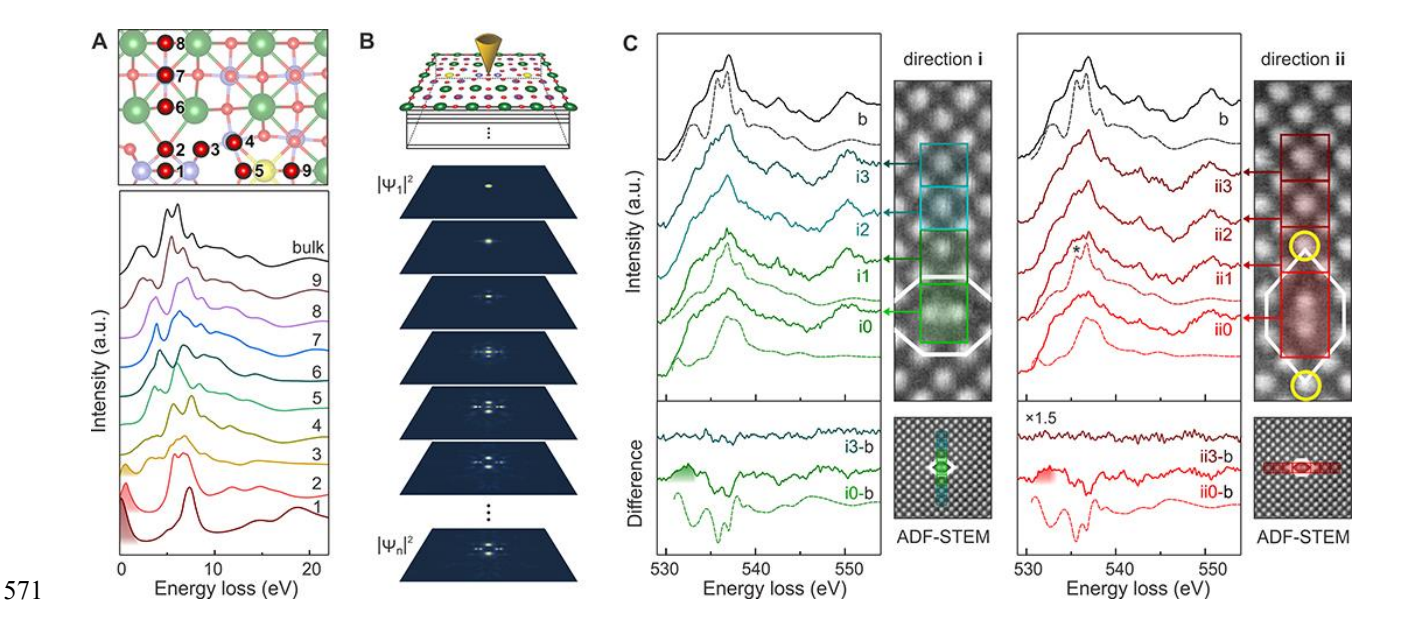


Fig. 4. EELS core-loss O K edges of the line defect. (A) Calculated O K edges for different O atoms in the line defect structure. The locations of these O atoms in the structure are indicated on the top panel. Peaks originated from metallic electronic states just above Fermi energy are highlighted with shading. (B) A schematic showing that when the STEM probe is located on an individual atomic column, by the time the beam propagates and exits the sample, it broadens and, therefore, measured EELS data should contain excitations from neighboring atomic columns. (C) Measured and simulated O K edges across the line defect in two perpendicular directions (i and ii). EELS acquisition areas are indicated in the right. The solid lines and dashed lines represent experimental data and simulations, respectively. Label 'b' indicates bulk. Enhanced peak due to bonding with La is marked with an asterisk. Simulated edges contain intermixing from neighboring oxygen atoms. Difference spectra between local and bulk O K edge spectra are shown in the bottom. Features corresponding to metallic electronic states just above Fermi energy are highlighted with shading.

Science Advances Manuscript Template Page 24 of 24

Supplementary Materials for

Metallic line defect in wide-bandgap transparent perovskite BaSnO₃

Hwanhui Yun, Mehmet Topsakal, Abhinav Prakash, Bharat Jalan, Jong Seok Jeong, Turan Birol, K. Andre Mkhoyan*

* Corresponding author. Email: mkhoyan@umn.edu

This PDF file includes:

Figs. S1 to S10

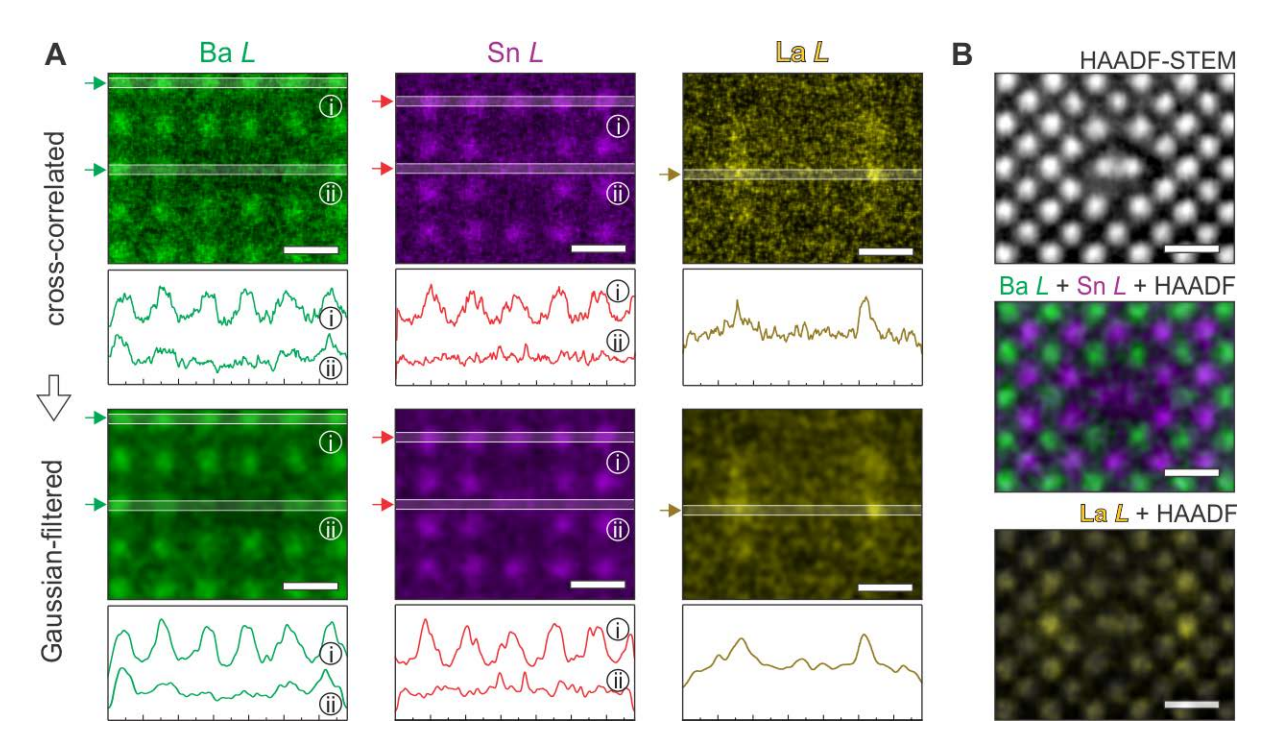


Fig. S1. Image processing of EDX elemental maps. (A) The steps showing how several EDX elemental maps acquired from a line defect were first cross-correlated and then Gaussian-filtered using full-width half maximum (FWHM) of 0.6 Å, which is below the spatial resolution of the STEM. The intensity line profiles extracted from the maps, presented below each map, show reduction of the noise in the maps. The locations of extracted line profiles are indicated by white lines and arrows on the maps. **(B)** Final EDX maps of Sn with Ba and La overlaid with a corresponding HAADF-STEM image. Scale bars are 0.5 nm. These final maps are the maps shown in main text, Fig. 1(**D**).

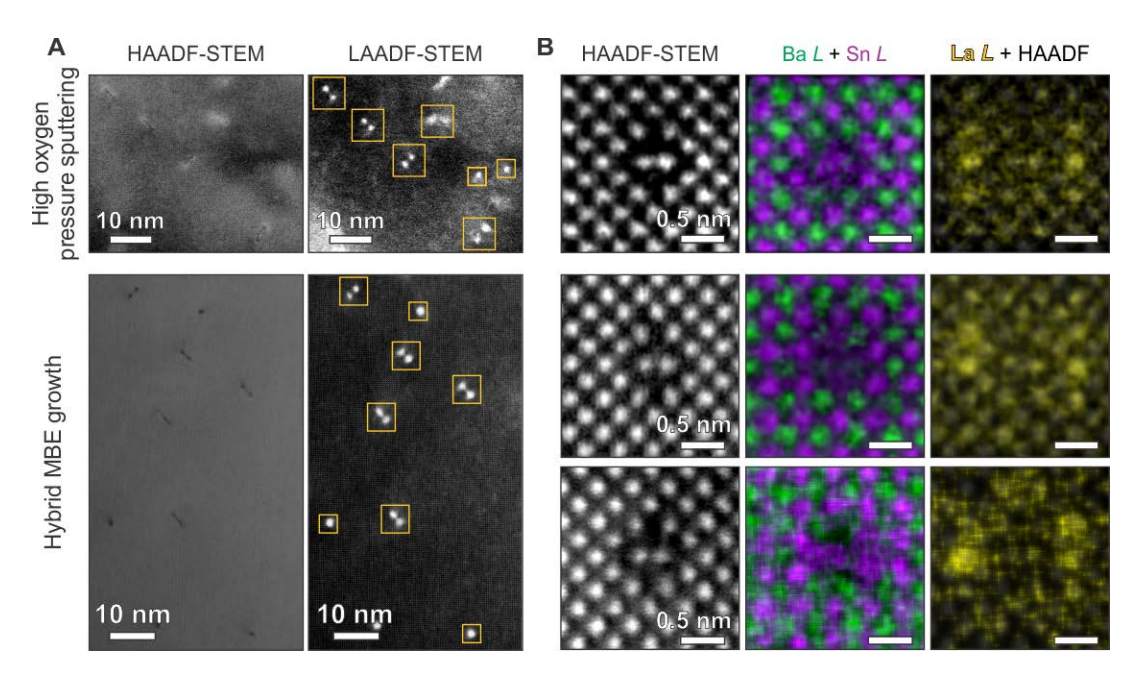


Fig. S2. ADF-STEM images and EDX elemental maps of the line defect. (A) Low-magnification planview HAADF- and LAADF-STEM images of La:BaSnO₃ thin films grown by high oxygen pressure sputtering and hybrid MBE techniques. LAADF-STEM images show presence of many strong spot-like contrast (highlighted in yellow boxes) in all BaSnO₃ films. HAADF-STEM images reveal that the contrast originates from either threading dislocations or these line defects. The density of the line defect appears to be dependent on the growth techniques or the strain in the film: about 3×10² defect/μm² for sputtering-grown La:BaSnO₃ films with high strain distribution, and about 30 defect/μm² for hybrid MBE-grown La:BaSnO₃ films with low strain distribution, based on LAADF image analysis. **(B)** Examples of atomic-resolution HAADF-STEM images and corresponding EDX elemental maps of line defects found in sputtering- and hybrid MBE- grown films, where Sn signal at the core and La signal at nearby atomic sites are visible in all cases.

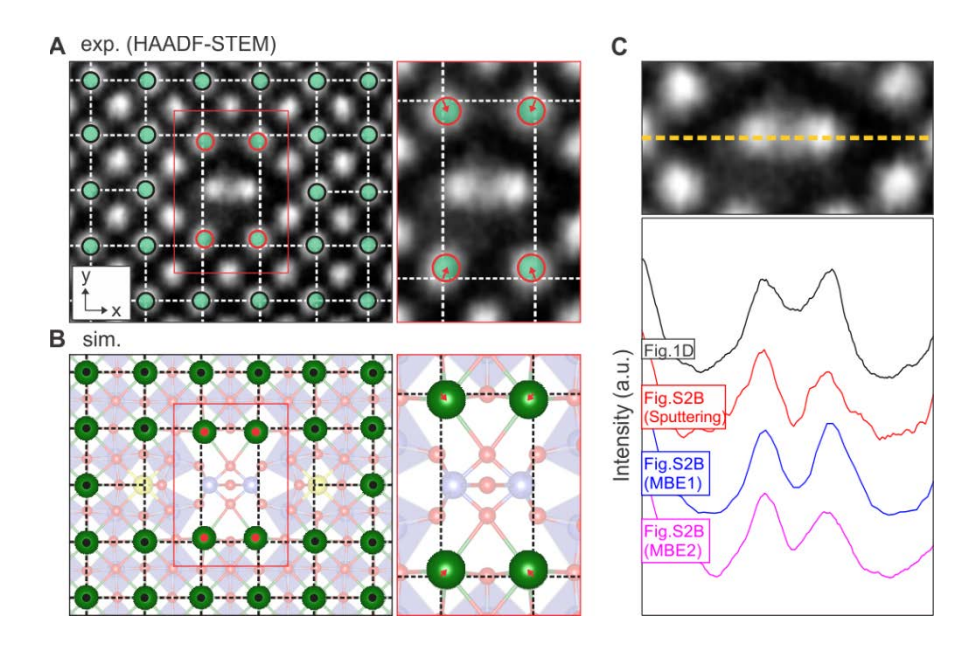


Fig. S3. Displacements of four neighboring Ba columns toward the defect core. (A, B) Experimental HAADF-STEM image and simulated atomic structures of the line defect showing inward displacement of the four neighboring Ba columns. Dash-lines connecting Ba atoms away from the defect core are drawn to visualize the displacement of four neighboring Ba columns relative to their bulk lattice sites. In the magnified images, displacements are indicated by red arrows. Inward displacements of the Ba columns in x- and y-directions were 6% and 15% (experiment) and 5% and 6% (simulation). (C) Intensity line profiles from the experimental HAADF-STEM images in Fig. 1(D) and SM Fig. S2(B) taken across core Sn-Sn pairs of a line defect as shown by a dashed line on the top image. These intensity profiles show variations in intensities in center O atom location as well as in core Sn locations suggesting variations in position and composition of these atomic columns.

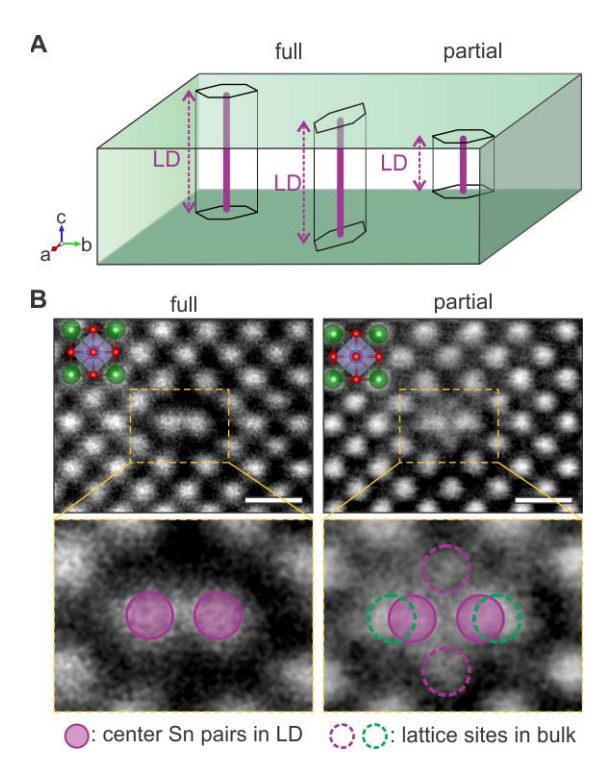


Fig. S4. Full and partial line defects. (A) Illustration of full and partial line defects. **(B)** HAADF-STEM images of full and partial line defects. HAADF-STEM image of the partial line defect shows superimposed contrast of the line defect and bulk BaSnO₃. Scale bars are 0.5 nm.

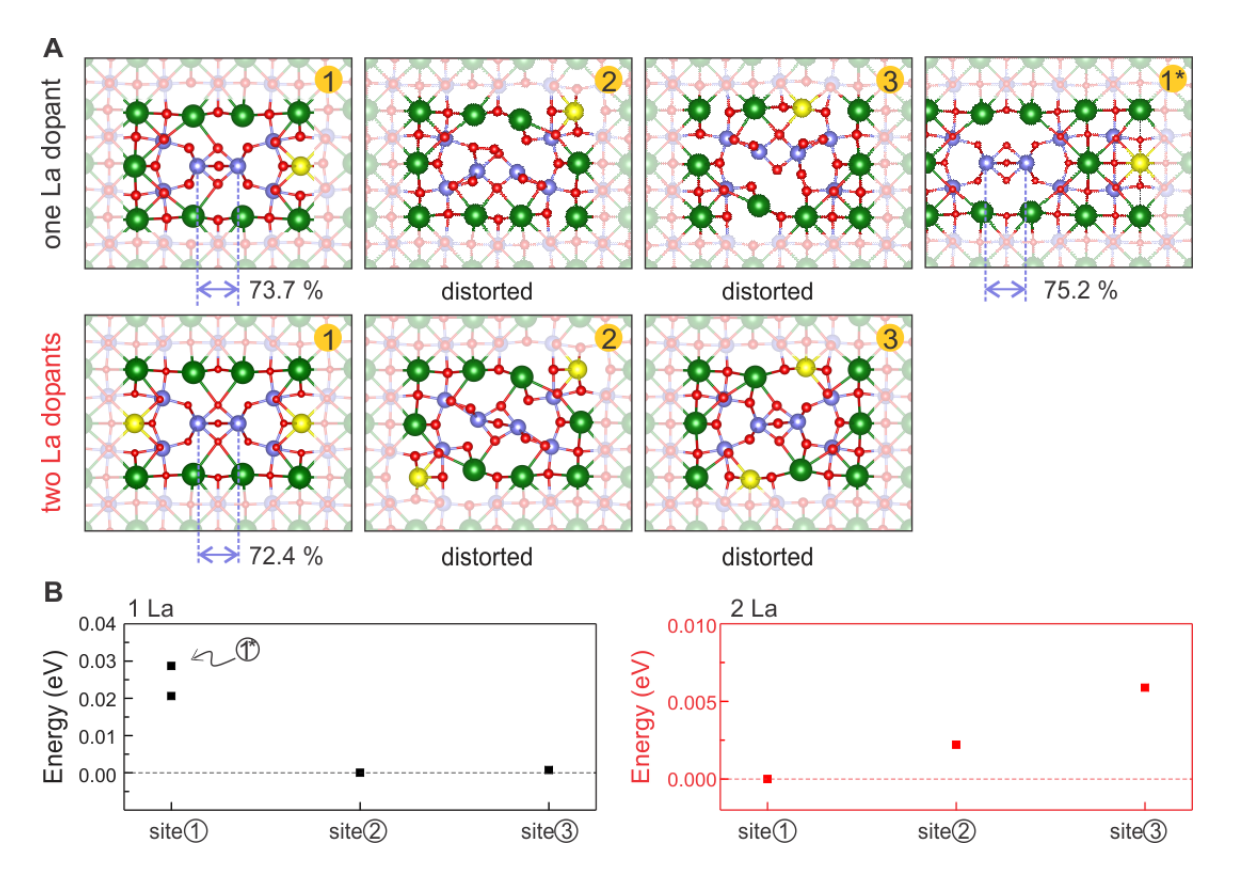


Fig. S5. The structure of the line defect with La dopant at different locations. (A) The relaxed atomic structure of the line defect with 1 La dopant (first row) and with 2 La dopants (second row). As La dopants substitute Ba atoms at the position Ba①, the core Sn-Sn distance reduces. (B) The relative total energy of each configuration. When comparing one La substitution at Ba① and Ba①* sites, substitution at Ba① site results in lower energy, which indicates the stabilizing effect of La dopants on the line defect when they are close. With only one La dopant, the total energy is lower when La is at sites Ba② or Ba③. However, they lead to asymmetric configurations and dangling oxygen atoms. With 2 La dopants, the defect core is energetically favorable when dopants are at the site Ba①, which is also closer to the experimental observations. When 2 La dopants are located symmetrically at position Ba② or Ba③, as shown in (A), the structure is distorted, but does not introduce dangling oxygen atoms. Based on total energies of the 2 La-doped line defect structures, La will be preferably be located in the order of: Ba①, Ba②, and Ba③ sites, which is consistent with the experimental observations.

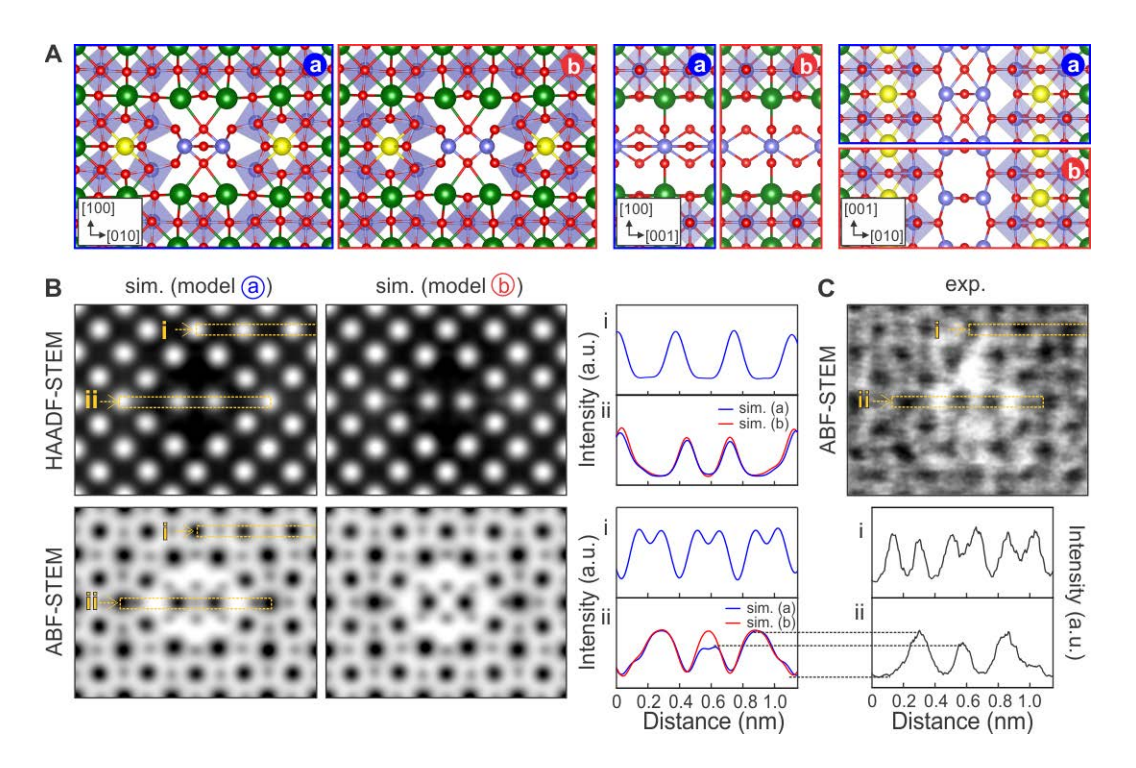


Fig. S6. The structure of line defect with and without oxygen in-between the Sn-Sn pair in the core. (A) The atomic structures of line defects after structural relaxation of the models with ⓐ and without ⓑ central oxygen atom, viewed along three major axes. The core Sn-Sn distance of the relaxed structures was 0.724a₀ and 0.734a₀ for ⓐ and ⓑ cases, respectively. (B) Simulated HAADF- and annular bright-field (ABF)-STEM images of two line defect structures shown in (A). *Multislice* algorithm was used for these simulations. Intensity line profiles were extracted from the bulk BaSnO₃ region (i) and the line defect region (ii), as indicated by yellow dotted lines, and plotted on the right panels. While simulated HAADF-STEM images of the two models do not show obvious difference, ABF-STEM images show visible contrast difference at the defect core due to darker contrast generated from the central oxygen. (C) Experimental ABF-STEM image of the line defect. The intensity line profile across the line defect core shows lower intensity at the center, which indicates that the structure likely contains oxygen atoms at the center.

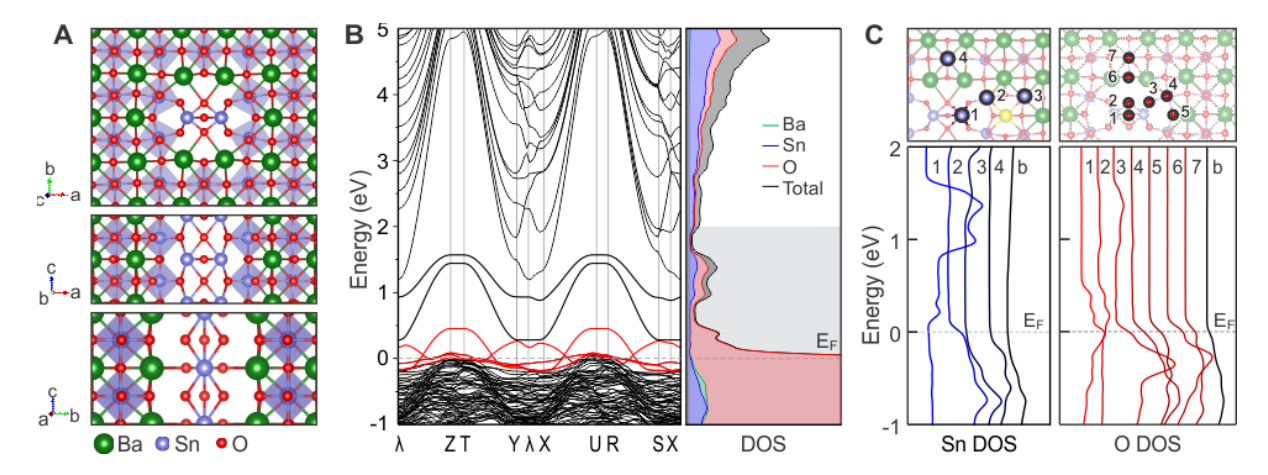


Fig. S7. Computed atomic and electronic structures of the line defect with no dopants. (A) Calculated atomic structure of the line defect viewed along three major axes. The Sn atoms in the defect core are shifted half unit cell along the defect line direction. The calculations also predict minor changes in the atomic structure of the BaSnO₃ structure outside defect core (e.g. an octahedral tilt in the surrounding four SnO₆ when viewed in the c-axis). (B) Electronic band structures and DOS of the line defect calculated using atomic structure in (A). Metallic bands, the bands that are crossing Fermi energy ($E_F = 0$) are highlighted in red. Atom-projected DOS indicate that the metallic bands are predominantly from O and Sn atoms. (C) Site-projected DOS for Sn and O atoms in the line defect structure. DOS of selected atoms, locations of which are indicated in the schematics on the top, show that the O and Sn atoms of defect core are the ones with metallic characteristics.

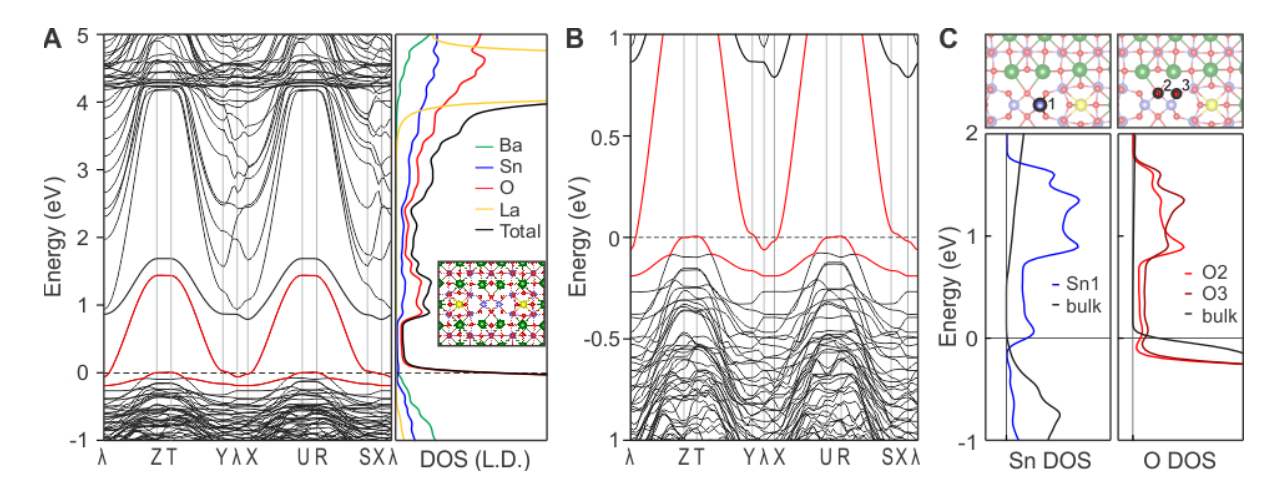


Fig. S8. Computed electronic structures of the line defect with O vacancy at the center. (A) Electronic band structure (left) and DOS (right) of the line defect with missing center oxygen. The atomic model is shown in the inset in the DOS plot. (B) Magnified band structure showing E_F -crossing bands. Metallic bands, the bands that are crossing Fermi energy ($E_F = 0$) are highlighted in red. (C) Site-projected DOS for core Sn and O atoms. DOS of selected atoms, locations of which are indicated in the schematics on the top, show that the O and Sn atoms of defect core are the ones with metallic characteristics.

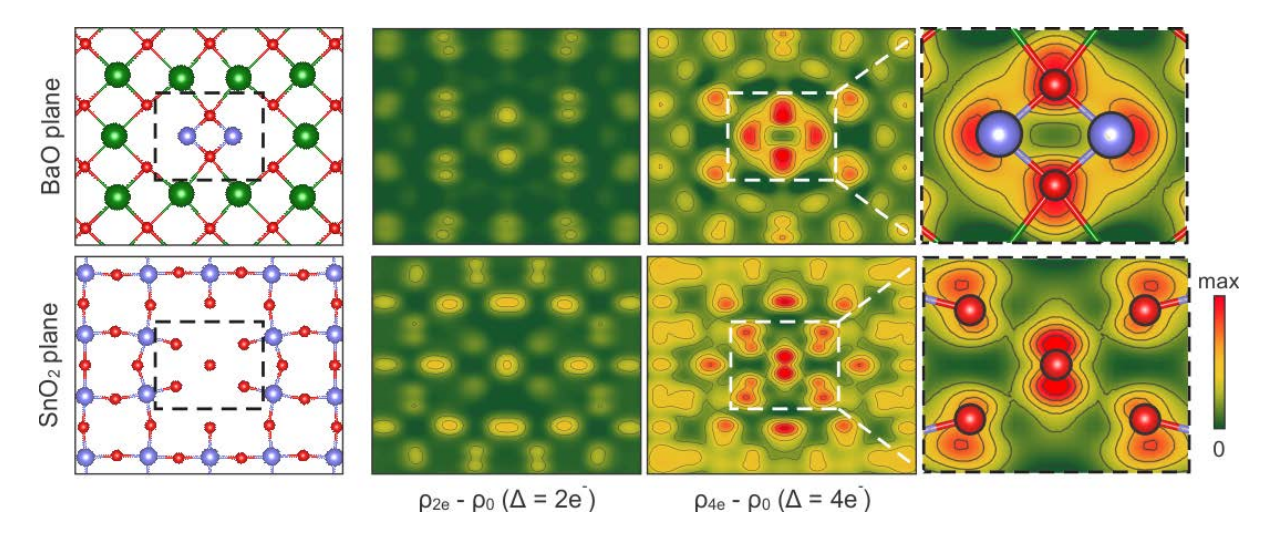


Fig. S9. The effect of additional negative charge on the line defect with no dopants. The atomic arrangements (on the left) and corresponding EDDMs between the additionally charged, with 2e⁻, 4e⁻, and original line defects without La dopants (on the right) for both atomic planes (BaO and SnO₂ planes) perpendicular to defect line direction. Magnified EDDMs of the defect core overlaid with atom model show that most of the additional charge is concentrated at the core O and Sn atoms. Undoped line defect with additional 4e⁻ is similar to 2-La-doped line defect with additional 2e⁻, shown in the main text, Fig. 3(B).

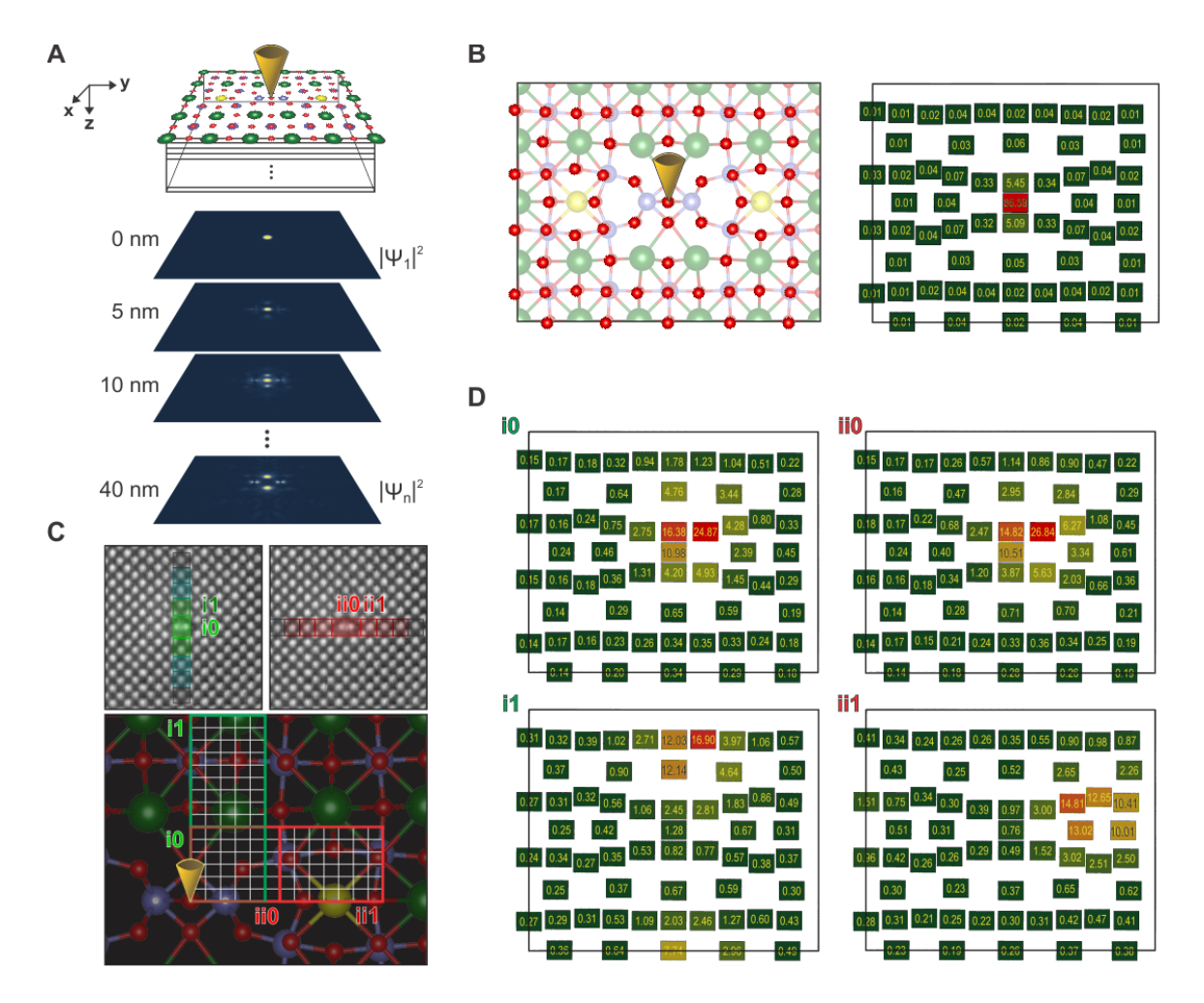


Fig. S10. Evaluation of O K edge intermixing in STEM-EELS spectra. Using Multislice algorithm, STEM beam propagation in the line defect structure was evaluated and contributions of core-electron excitation from individual oxygen atoms were determined. (A) The electron beam intensity distribution at each depth was computed, as shown schematically for a probe located at the center of the line defect. Slice thickness of $\Delta z = 2.055$ Å, which is a half of the unit-cell, was used in these simulations and the total thickness of the structure was set to be 40 nm. Beam intensity at each oxygen atom was evaluated by integrating the intensity within the radius of oxygen atom ($r_0 = 0.73 \text{ Å}$). (B) The atomic structure of the line defect with highlighted oxygen atoms used for the integration (left) and the oxygen atom-projected beam intensity map for the probe located at the center (right). On the map, fractions of the beam intensity at each O atomic column (in %) are indicated. In this case of a STEM probe located at the center, final O K edge is determined by a weighted average of O K edges from the all O atoms on this map with fractions used as weighting coefficients. O K edges used for such calculations are shown in Fig. 4(A). For O atoms outside the displayed region, bulk O K edge was used. (C) To account for the scanning probe in each area used for EELS acquisition, the acquisition areas (i0, i1, ii0, and ii1) were meshed to generate evenly distributed probe positions (with step size of 0.5 Å). The oxygen atom-projected beam intensity maps were calculated for each probe position and averaged for each region. (D) The final oxygen atom-projected beam intensity maps for each EELS acquisition areas: i0, i1, ii0, and ii1. Fractions of the beam intensity (in %) are indicated at O atomic columns on each map. By calculating a weighted average of O K edges based on the fractions, the O K edge spectra for the areas i0, i1, ii0, and ii1 were determined and used in main text, Fig. 4(C).